# Fiducial-aided calibration of a displacement laser probing system for in-situ measurement of optical freeform surfaces on an ultra-precision fly-cutting machine

SHIXIANG WANG,[1] CHI FAI CHEUNG,[1,*] [iD] LINGBAO KONG,[2] [iD] AND MINGJUN REN[3] [iD]

[1] *State Key Laboratory of Ultra-Precision Machining Technology, Department of Industrial and Systems Engineering, The Hong Kong Polytechnic University, Kowloon, Hong Kong, China*
[2] *Shanghai Engineering Research Center of Ultraprecision Optical Manufacturing, Fudan University, Shanghai, China*
[3] *School of Mechanical Engineering, Shanghai Jiao Tong University, Shanghai, China*
*\*benny.cheung@polyu.edu.hk*

**Abstract:** Surface metrology is an essential operation to determine whether the quality of manufactured surfaces meets the design requirements. In order to improve the surface accuracy and machining efficiency in the manufacturing of optical freeform surfaces, in-situ surface measurement without re-positioning the workpiece is considered as a promising technique in advanced manufacturing. In this study, a displacement laser scanner is integrated into an ultra-precision fly-cutting machine in order to perform as a coordinate measuring machine. However, some inevitable errors such as motion errors of the machine tool, thermal drift, vibrations, and errors of the laser sensor are introduced due to the manufacturing environment. To improve the performance of the measurement system, calibration of the main error sources is investigated with consideration of the characteristics of the built laser scanner system. Hence, the relationship between the moving speed of the laser scanner and the vibration of the tested signals is studied. Following that, the errors of the $z$-axis scale could be corrected by measuring a four-step heights artefact. Furthermore, volumetric positioning errors are identified by the proposed modified chi-square method and Gaussian processing prediction method. Simulation and measurement experiments are conducted, and the results indicate that the calibrated measuring system can measure ultra-precision freeform surfaces with micrometre form accuracy.

## 1. Introduction

Surface topography measurement plays a key role in the ultra-precision manufacturing field for quality control and further machining process improvement. A large variety of off-line surface metrology instruments which are typically set in a well-controlled environment are used to acquire surface information, such as coordinate measuring machine (CMM), stylus profiles [1] and non-contact optical instruments [2]. With the increasing geometric complexity of ultra-precision freeform surfaces, such as manufacturing micro/nano-structured surfaces [3], off-line surface measurement cannot meet the requirements. This is particularly true when the same workpiece needs to be re-mounted to carry out the measurement of and compensation for machining errors. In order to ensure the surface quality of the workpiece, an in-situ measurement system that incorporates measurement sensors into ultra-precision machine tools provides a promising solution, which not only avoids post-process inspection, but also makes compensation machining easy to be carried out. However, due to the measurement sensors always moving along the axes of the machine tool, the spindle and slide error motions, vibration of the integrated measuring components and the machine tool itself, thermal drift and also the errors of the sensor adversely affect the uncertainty of the in-situ measurement applications.

Recently, many researchers have paid attention to the development of in-situ measuring instruments for precision machine tools. Li et al. [4] developed an in-situ autostereoscopy-based 3D measuring system to measure the micro-structured surfaces on an ultra-precision turning lathe. The system consisted of a microlens, a CCD sensor and a group of LED light bars to acquire the 3D raw information and extract disparity data from an established 3D digital model under different working environments. One limitation of this study was the resolution of measurement. Zhang et al. [5] employed a fringe deflectometry system both on a five-axis ultra-precision machine and a Taylor Hobson 1250GPI profilemeter. By using the fringe patterns, the phase similarity and phase range of the fringes were used to identify the position information. The linear and tilted positioning accuracy can be lowered to 5 μm and 0.005°, respectively. The measurement results were influenced by the fringe pattern accuracy as well as the positions between the light screen and the camera but there is still not adequate knowledge to address these problems.

In addition, a scanning tunnelling microscope was integrated into a diamond machine to manufacture and characterize the pyramid array surface [6]. The uncertainty of this in-situ measurement system was also analyzed. Li et al. [7,8] presented an interferometric on-machine probing system on a three-axis diamond turning machine. System errors such as kinematic error and vibration of the machine tool were also investigated and calibrated. Some contact probes with low measuring force were also applied to inspect the optical surface. The in-situ displacement probes were usually supported by an air bearing, so the displacement could be measured by a linear variable differential transformer (LVDT) [9–11]. Xu et al. [12] studied the LVDT on a three-axis ultra-precision machine tool and measured the sinusoidal surface. They successfully carried out the surface compensation process and achieved good results. Ito et al. [13] mounted a specular laser triangulation sensor on an ultra-precision grinding machine tool to measure the ceramic parts and the measurement errors including motion errors, tilt error and stability error. Chen et al. [14] designed a new chromatic confocal configuration to divide the reflected laser beam into two sub-beams so that the spectral non-smoothness of the mode-locked laser source can be eliminated. Seewig et al. [15] proposed that the use of scattered light sensors can be a powerful technique to measure form accuracy and surface roughness for in-line measurement. Tereschenko et al. [16] presented a passive vibration compensation method by integrating a high-resolution distance measuring interferometer into the white-light interferometer so that the measured deviations from the depth-scanning can be used to correct the measurement by the white-light interferometer.

Most of these studies focused on the task of in-situ measurement such as evaluation of the manufactured surface, compensation process, etc. On the contrary, separation and reduction of the additional error sources of these sensors as well as the related calibration in each type of in-situ measurement system have received little attention. As a result, this paper presents an in-situ displacement probing system which is integrated on a five-axis ultra-precision machine. It shows the calibration strategy for the volumetric errors, $z$-axis scale errors as well as the vibration influence.

## 2. Calibration of the integrated in-situ probing system

### 2.1. Development of the in-situ displacement probing (ISDP) system

In this study, a laser displacement probe was integrated onto a 5-axis ultra-precision fly-cutting machine (Precitech Freeform 705G, USA) including three linear axes and two rotary axes to perform as a coordinate measuring machine ($x$, $y$, $z$ information). The high quality of the displacement sensor (Keyence, LK-G5000), with 20 nm measurement repeatability and ± 0.02% linearity in terms of the 2 mm measuring range with a 25 μm spot diameter at standard distance [17] provides the feasibility of measurement in ultra-precision technology. In this study, the measurement information was achieved by inspecting the positions of the three moving linear

axes of the ultra-precision machine and the signals were loaded from the displacement sensor in the $z$ direction.

As shown in Fig. 1, the displacement laser sensor is mounted on the spindle so that it can move along the $x$ axis and $y$ axis and obtain the displacement information in the $z$ axis direction. To improve the measurement preference, the direction of the laser light should be aligned to the $z$ direction of the $z$ axis on the machine tool as accurately as possible although the measurement results are different from the reference distance which is determined by the sampling frequency of the sensor. In addition, the relative position distance of the laser sensor and the fly-cutting centre was set as about 40 mm, 5 mm, and 5 mm in the $x$, $y$, and $z$ directions respectively so as to avoid interference when the length of the machined workpiece is less than 40 mm and the height difference ($z$ direction) is larger than 5 mm simultaneously. To further ensure the alignment of the laser scanner, a transformation matrix [18] was identified with measurement of a few known surfaces so as to unify the coordinate frame of the sensor and the tool tip. In order to ensure the working space of the ISDP system, the space centre of the machine tool was set as the start point in the machine tool coordinate frame. Furthermore, the $z$-axis does not move in the whole measurement process after the stand distance is identified. Considering the one-dimensional property of the laser scanner, only a uni-directional scanning tool path as shown in Fig. 1 was selected so that the $x$, $y$ positions could be consistent with the $z$ displacement.
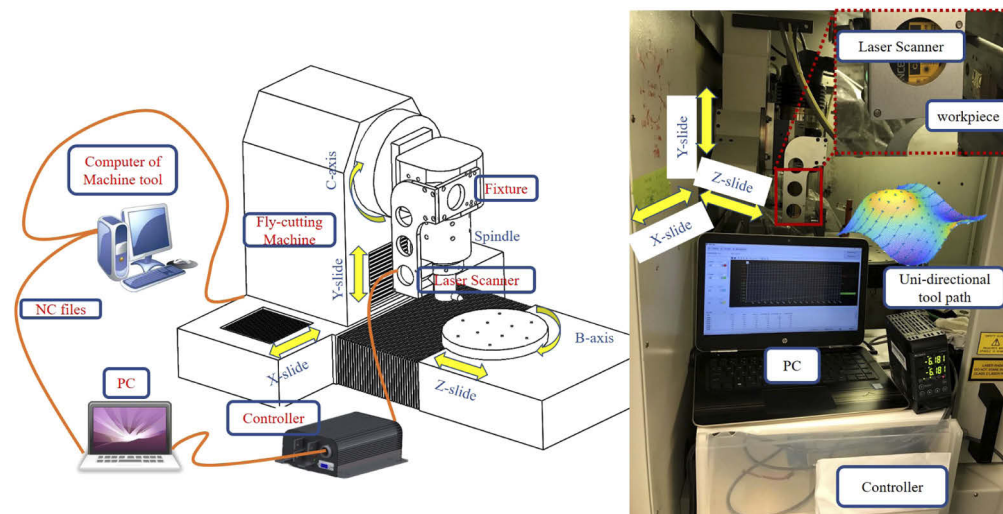


**Fig. 1.** Diagram of the developed in-situ displacement probing system.

According to the configuration of the developed ISDP system, only the $z$ direction is of interest because the $x$ direction and the $y$ direction can be guaranteed by the ultra-precision linear scale feedback with as small as 14 nm and 6 nm resolution [19], respectively. In order to evaluate the performance of the ISDP system, three factors that can influence the measurement accuracy including vibration of the integrated measuring components and the $z$ axis scale errors and volumetric errors of the machine tool, they were determined and calibrated as compared with the corresponding results measured on the off-line measurement instrument.

## 2.2. Errors of the volumetric positioning

The developed ISDP system moves along the axes of the machine in order to carry out the metrology task. It is inevitable that measurement errors occur due to errors stemming from the geometric errors of the machine tool, inaccuracies in assembly, wear of the components, the

errors of the probing system and so on. It is quite complex to identify the individual errors from one to the other. The comprehensive effect of all these errors are considered as volumetric positioning error. To obtain the combined errors in the machine tool, a fiducial-aided positioning method [18] was employed. A reconfigurable calibrated fiducial-aided artefact was measured in a relatively high-precision machine tool and it was amounted in the working space of the machine tool. The nominal positions of these fiducials were assured to be $T_{np}$, read from the numerical control system in the machine tool coordinate frame. However, due to the volumetric errors, these positions did not coincide with the calculated positions $T_{cp}$ which are regarded as actual positions transformed from the calibrated positions. Hence, the volumetric errors of the machine tool can be defined by the bias between the transformed positions of the calibrated fiducials and the measured positions in the machine tool coordinate frame, as given in Eq. (1):

$$E_v = T_{cp} - T_{np} \tag{1}$$

It is assumed that the volumetric errors are determined by the mean values along the $x$, $y$ and $z$ axes of the measuring system, the errors were set as $\varepsilon_{mX}$, $\varepsilon_{mY}$, $\varepsilon_{mZ}$, and a root sum square approach was used to obtain the volumetric error:

$$E_v = \sqrt{\varepsilon_{mX}^2 + \varepsilon_{mY}^2 + \varepsilon_{mZ}^2} \tag{2}$$

For the calibrated fiducial-aided artefact, it is considered that the errors between the position of the calibrated fiducials and the real positions of the fiducials in the calibrated measuring coordinate frame are much smaller than the errors obtained in the in-situ measuring system. However, these errors still need to be considered. Similarly, the combined errors are set as $\varepsilon_{rX}$, $\varepsilon_{rY}$ and $\varepsilon_{rZ}$ along the three moving axes. The relationship among those three coordinate frames and the definition of the several errors are shown in Fig. 2.
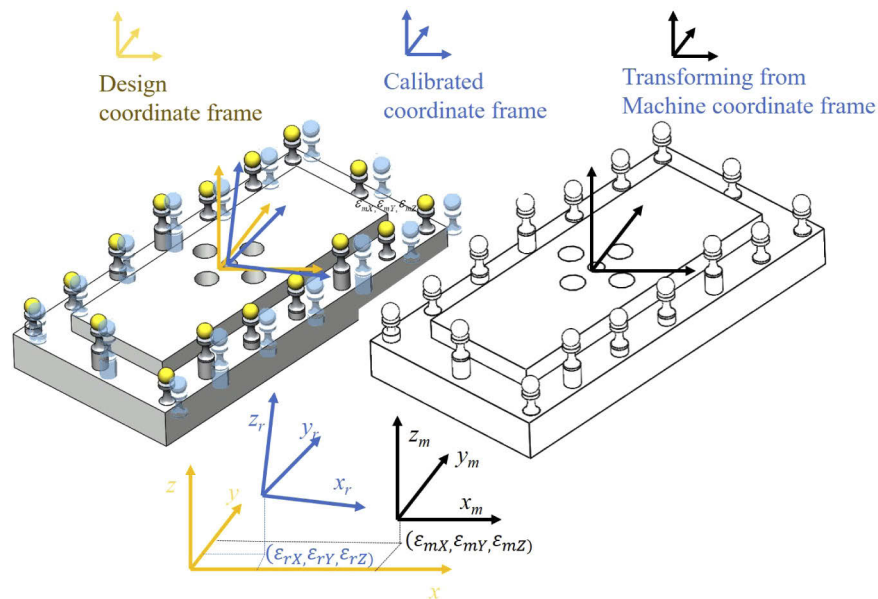


**Fig. 2.** Errors in different coordinate frames.

## 2.3. Modified chi-square volumetric error identification

A reconfigurable calibrated fiducial-aided artefact composed of a set of standard spheres was mounted on the machine tool. The individual spheres, $S_i$, $i = 1, 2 \cdots n$, set the calibrated positions

as $(X_{ri}, Y_{ri}, Z_{ri})$, so the positions of these spheres $(X_{ci}, Y_{ci}, Z_{ci})$ in the machine tool could be transformed from the calibrated coordinate frame and determined as follows:

$$
\begin{bmatrix} X_{ci} \\ Y_{ci} \\ Z_{ci} \end{bmatrix} = \begin{bmatrix} D_1 & D_2 & D_3 \\ D_3 & D_5 & D_6 \\ D_7 & D_8 & D_9 \end{bmatrix} \begin{bmatrix} X_{ri} \\ Y_{ri} \\ Z_{ri} \end{bmatrix} + \begin{bmatrix} D_x \\ D_y \\ D_z \end{bmatrix}
\tag{3}
$$

where $D_1, D_2 \cdots D_9$ are the fitted parameters and $D_x, D_y, D_z$ are the residual errors. However, in the actual measurement, the measured positions of the spheres $(X_{mi}, Y_{mi}, Z_{mi})$ in the machine tool were always not equal to the calculated ones because of the effect of the volumetric positioning errors and the measuring device error, so the theoretical relationship between the calculated positions and the measured datasets can be defined by a modified chi-square method [20],

$$
\chi^2 = \frac{1}{3N-8} \sum_{i=1}^{N} \left( \begin{bmatrix} X_{mi} \\ Y_{mi} \\ Z_{mi} \end{bmatrix} - \left( \begin{bmatrix} D_1 & D_2 & D_3 \\ D_3 & D_5 & D_6 \\ D_7 & D_8 & D_9 \end{bmatrix} \begin{bmatrix} X_{ri} \\ Y_{ri} \\ Z_{ri} \end{bmatrix} + \begin{bmatrix} D_x \\ D_y \\ D_z \end{bmatrix} \right) \right)
\tag{4}
$$

where $N$ is the total number of fiducials. The volumetric error of a machine tool is usually an-isotropic, which means that the errors are not uniformly located along each axis. Besides, considering that different fitting parameters in Eq. (4) would have different variances and covariances, weighting factors can be set to each axis based on the variance of the volumetric positioning errors so as to eliminate the heteroscedasticity [21]. Hence, a weighting matrix $W$ was used to improve the accuracy of the modified chi-square method, as given in Eq. (5):

$$
\chi^2 = \frac{1}{3N-8} W \sum_{i=1}^{N} \left( \begin{bmatrix} X_{mi} \\ Y_{mi} \\ Z_{mi} \end{bmatrix} - \left( \begin{bmatrix} D_1 & D_2 & D_3 \\ D_3 & D_5 & D_6 \\ D_7 & D_8 & D_9 \end{bmatrix} \begin{bmatrix} X_{ri} \\ Y_{ri} \\ Z_{ri} \end{bmatrix} + \begin{bmatrix} D_x \\ D_y \\ D_z \end{bmatrix} \right) \right)
\tag{5}
$$

where the weighting matrix is defined by $W = diag[1/\varepsilon_{mX}^2, 1/\varepsilon_{mY}^2, 1/\varepsilon_{mZ}^2]$. In order to find the best fitted parameters (bfp), $V_{bfp} = [D_1, \cdots, D_9, D_x, D_y, D_z]^T$, these parameters can be determined by vanishing the partial derivative of Eq. (5) to $V_{bfp}$, and by setting the results to zero, they can then be easily determined:

$$
\frac{\partial \chi^2}{\partial V_{bfp}} = 0
\tag{6}
$$

$$
V_{bfp} = B^{-1} \cdot R
\tag{7}
$$

where $B$ is a $12 \times 12$ matrix and $R$ is a column vector

$$
B = \begin{bmatrix}
Q_{3\times3} & 0 & 0 & F_{3\times1} & 0 & 0 \\
0 & Q_{3\times3} & 0 & 0 & F_{3\times1} & 0 \\
0 & 0 & Q_{3\times3} & 0 & 0 & F_{3\times1} \\
F_{3\times1}^{T} & 0 & 0 & N & 0 & 0 \\
0 & F_{3\times1}^{T} & 0 & 0 & N & 0 \\
0 & 0 & F_{3\times1}^{T} & 0 & 0 & N
\end{bmatrix}, \; R = \begin{bmatrix}
x_r x_m \\
y_r x_m \\
z_r x_m \\
\vdots \\
x_r z_m \\
y_r z_m \\
z_r z_m \\
x_m \\
y_m \\
z_m
\end{bmatrix}
\tag{8}
$$

$$
Q_{3\times3} = \begin{bmatrix}
x_r{}^2 & x_r y_r & x_r z_r \\
x_r y_r & y_r{}^2 & y_r z_r \\
x_r z_r & y_r z_r & z_r^2
\end{bmatrix}, \; F_{3\times1} = \begin{bmatrix}
x_r \\
y_r \\
z_r
\end{bmatrix}
\tag{9}
$$

For easy reading of the equations, the $\sum$ and the subscript are dropped, for instance, $z_r = \sum_{i=1}^{N} Z_{ri}$, $z_r^2 = \sum_{i=1}^{N} Z_{ri}^2$ and $y_r z_r = \sum_{i=1}^{N} (Y_{ri} Z_{ri})$. It is clear that Eq. (7) can be easily solved by using Cramer's Rule. From the above equations, it is obvious that the obtained best fitted parameters propagate new errors in the transforming process. A set of the errors of the 12 best fitted parameters are $\varepsilon_{D_j}, j = 1, \cdots 9, x, y, z$. The errors of these parameters can be defined by:

$$
\begin{aligned}
\varepsilon_{D_j}^2 = & \sum_{i=1}^{N} \left( \left( \frac{\partial D_j}{\partial X_{mi}} \right)^2 \varepsilon_{D_{mX}}^2 + \left( \frac{\partial D_j}{\partial Y_{mi}} \right)^2 \varepsilon_{D_{mY}}^2 + \left( \frac{\partial D_j}{\partial Z_{mi}} \right)^2 \varepsilon_{D_{mZ}}^2 \right) \\
+ & \sum_{i=1}^{N} \left( \left( \frac{\partial D_j}{\partial X_{ri}} \right)^2 \varepsilon_{D_{rX}}^2 + \left( \frac{\partial D_j}{\partial Y_{ri}} \right)^2 \varepsilon_{D_{rY}}^2 + \left( \frac{\partial D_j}{\partial Z_{ri}} \right)^2 \varepsilon_{D_{rZ}}^2 \right)
\end{aligned}
\tag{10}
$$

As studied in previous work [20], the errors of the fitted parameters can be obtained by determining the inverse matrix *B*, and they could be very small and up to 0.016 µm.

The relationship among different Cartesian coordinate systems is confirmed by the built mathematical model by using a number of fiducials. To check the accuracy of the proposed mathematical model, a Monte Carlo simulation method [22,23]was used to check how many fiducials could achieve better performance with a relatively high accuracy. Figure 3 shows the mean value and standard deviation of the simulated volumetric errors after 3,000 repeated experiments with different fiducials.

As shown in Fig. 3, the volumetric errors are almost equal to zero when using three or four fiducials but the values are significantly increased with an increasing number of fiducials from five to 13, and a slow increase can be seen when the number of fiducials increase to 20. After that, the values of the volumetric errors display a stable trend. It is obviously shown that the volumetric errors may be hidden if less than four fiducials are used but the volumetric errors are measured if more than 20 fiducials are used. It was concluded that 24 fiducials could achieve good results in the assessment of the volumetric error in this study.

## 2.4. Prediction and compensation of the volumetric errors in the working space

In the developed mathematical model, the volumetric errors can only be obtained at several measurement points. The other errors in the remaining positions can be determined by
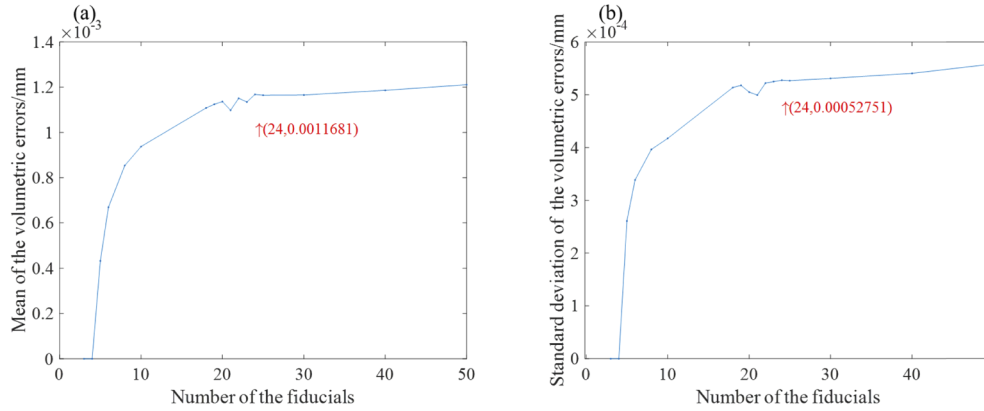
**Fig. 3.** The mean value and standard value of the volumetric errors.

interpolation. To generate numerous spatial measurements that cover the entire working space, a Gaussian Process (GP) modelling method was used to predict the volumetric positioning errors with high accuracy. The GP modelling method is a powerful tool in machine learning, and it provides a Bayesian nonparametric approach to smoothing and interpolation [24].

It was assumed that the calculated volumetric errors at the nominal position $p = (x, y, z)$ is $V_e$, and these nominal positions and their errors were set as the input and output parameters of the GP model. A linear system with Gaussian distribution error with zero mean and $\sigma_n$ standard deviation is given in Eq. (12):

$$V_e = f(p) + N \sim (0, \sigma_n) \tag{11}$$

Then the 'real' volumetric errors $f(p)$ can be defined by a mean function $\mu(p)$ and a covariance function $K(p, p)$ in the GP model:

$$f(p) \sim GP(\mu(p), K(p, p)), \tag{12}$$

So the $V_e$ can be determined by the input positions as:

$$V_e \sim N(0, K(p, p) + \sigma_n I) \tag{13}$$

where $I$ is the identity matrix. So the joint distribution over the calculated $V_e$ at the training position $p$, and the predicted $V_e^*$ at the test position $p^*$ is thus given by Eq. (14):

$$\begin{bmatrix} V_e \\ V_e^* \end{bmatrix} \sim N \left( 0, \begin{bmatrix} K(p, p) + \sigma_n I & K(p, p^*) \\ K(p^*, p) & K(p^*, p^*) \end{bmatrix} \right) \tag{14}$$

where $K(p, p)$ and $K(p^*, p^*)$ are the variance-covariance matrix at the training locations and predicted locations, and $K(p, p^*)$ and $K(p^*, p)$ are the covariances between the Gaussian process evaluated at the training and predicted sets $p$ and $p^*$. As a result, the predicted volumetric errors can be determined as:

$$V_e^* | p^*, p, V_e, \theta \sim N(\overline{V_e^*}, cov(V_e^*)) \tag{15}$$

where the mean function is:

$$\overline{V_e^*} = K(p^*, p^*) - K(p^*, p)[K(p, p) + \sigma_n I]^{-1} K(p, p^*) \tag{16}$$

and the covariance function is:

$$cov(V_e^*) = K(p^*, p)[K(p, p) + \sigma_n I]^{-1} V_e \tag{17}$$

where $\theta$ is the hyperparameter given by the covariance kernel. In the GP model, the zero mean function is usually chosen because of the lack of available prior information about the volumetric errors. Hence, the heart of the GP model is the covariance kernel optimized by the hyperparameters. In this study, a spectral mixture kernel is defined by Eq. (18):

$$K(t, t') = \sum_{q=1}^{Q} w_q \cos(2\pi \boldsymbol{\mu}_q^T (t - t')) \prod_{m=1}^{M} e^{-2\pi^2 (t-t')_m^2 v_q^{(m)}} \tag{18}$$

where $t$ and $t'$ are any pairs of the inputs with $M = 3$ dimensions, $Q = 10$ is the total number of the mixture kernels, $\theta(w_q, \boldsymbol{\mu}_q, v_q^{(m)})$ are the hyperparameters, which include the $qth$ component which has the mean vector $\boldsymbol{\mu}_q = (\mu_q^1, \ldots, \mu_q^{(M)})$and covariance matrix $v_q^{(m)} = diag(v_q^{(1)}, \ldots v_q^{(M)})$, and $w_q$ are mixture weights. A marginal likelihood function Eq. (19) was used to achieve the optimized hyperparameters.

$$log(p(V_e | V_e^*, \boldsymbol{\theta})) = -\frac{1}{2} \boldsymbol{V}_e^T (K(\boldsymbol{p}, \boldsymbol{p}) + \sigma_n \boldsymbol{I}) - \frac{1}{2} log|(K(\boldsymbol{p}, \boldsymbol{p}) + \sigma_n \boldsymbol{I}| - \frac{1}{2} log 2\pi \tag{19}$$

After building and training the GP model, the prediction volumetric errors at the corresponding positions in the working space were obtained. Figure 4 shows a schematic diagram of the prediction process based on the GP model.
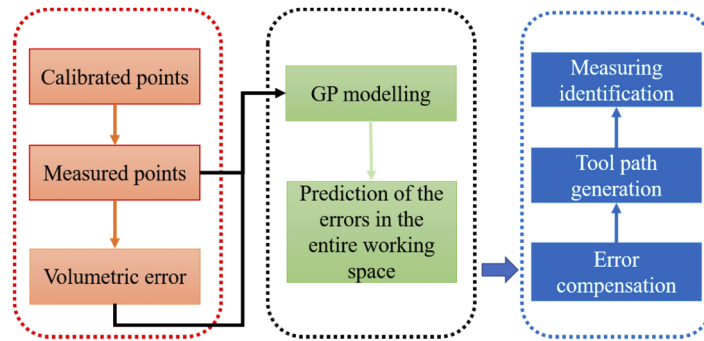


**Fig. 4.** Diagram of the GP-based prediction model.

A simulation study was carried out to check the accuracy of the GP-based prediction model. A total of 24 arbitrary points were generated and a standard error of 0.2 μm was added in three directions so that these points could be simulated as the calibrated points. The measured points could be obtained by adding several errors in the three directions, including probing errors (0.2,0.2,0.5)μm, and determining the centre of the standard sphere (0.3,0.3,0.5)μm, geometric error (0.5,0.5,0.8)μm, and thermal error (0.1,0.1,0.1)μm, by transforming the calculated points with an arbitrary transformation matrix. Hence, the volumetric errors of these 24 positions were determined by substituting them into Eq. (7). After setting the measured points and volumetric errors as input and output of the GP model, respectively, the prediction errors in the entire working space could be modelled. Finally, the compensation process was finished by changing the tool path in the new measurements. Figure 5 shows the results of the predicted volumetric errors and the calculated errors at the same position after 100 repeated simulations.

According to the results of Fig. 5, the deviation between the two datasets was drawn as shown in Fig. 6. The mean value of the prediction errors and the calculated errors are both 1.5 μm and the maximum value of the deviation is less than 0.0096 μm. These results show that the GP model has relatively high accuracy regarding the prediction of volumetric errors.
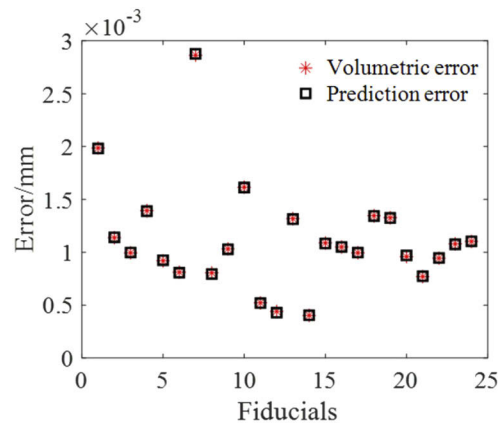
**Fig. 5.** Prediction errors and volumetric errors at 24 positions.

### 2.5. Vibration estimation of the measuring system

There are three main types of machine tool vibrations [25] including random vibrations due to impulsive loading of the machine tool, forced vibrations due to spindle imbalance and electric motors, and self-induced vibrations due to the feed motion or cutting process. These vibrations have a significant influence on ultra-precision freeform surface machining and the measuring process. It is necessary to reduce or eliminate them with consideration of the sampling strategies [26].

For the developed measuring system, the vibrations are due to interaction of the dynamic behaviour of the measuring process, which means that these two parameters – feed rate of the scanning speed and sampling frequency of the sensor – should be tested and optimized according to the measured surface. In order to avoid aliasing, it is necessary to have the sampling frequency two times more than the vibration frequency of the machine tool [27]. In addition, according to the analysis of the vibrations in an interferometric measuring system [8], it is suggested that the feature frequency of the measuring surface of interest should be lower than the vibration frequency. In this study, the vibration source was mainly considered as the dynamic behaviour of
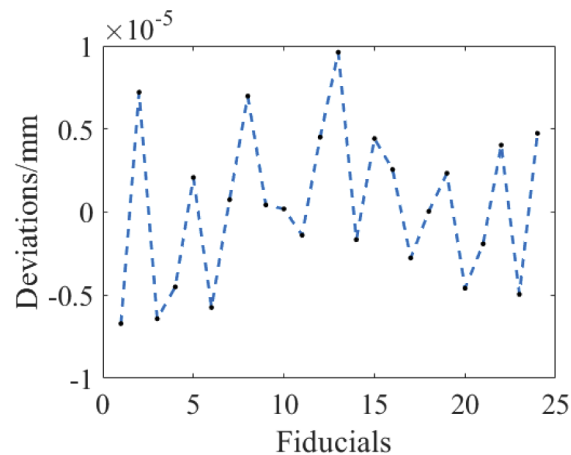


**Fig. 6.** Deviation between the prediction error and the calculated datasets.

the developed on-machine device. It is important to find the relationship between the scanning speed and the vibration.

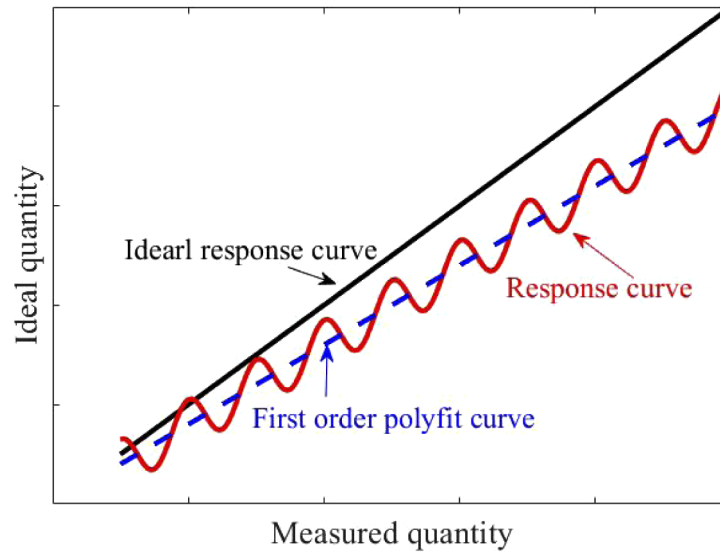## 2.6. Calibration of z-axis scale errors



**Fig. 7.** Instrument response curve to correct the amplification coefficient and linearity.

Due to the environmental effects, especially temperature and metrological characteristics between the ideal quantity and measured quantity, the amplification coefficient and linearity of the z-axis scale need to be considered. Matthias et al. [28,29] proposed manufacturing of new roughness standard for the linearity of the vertical axis and they achieved a good result. However, this method needs to measure the surface roughness which is not applicable for the displacement sensor. In this study, the instrument response curve [30] method as shown in Fig. 7 was used to correct the amplification coefficient and linearity of the sensor at the *z*-axis. The amplification coefficient was defined as the first-order poly-fit value of the response curve, and the linearity was obtained from the maximum local deviation of the response curve. To achieve
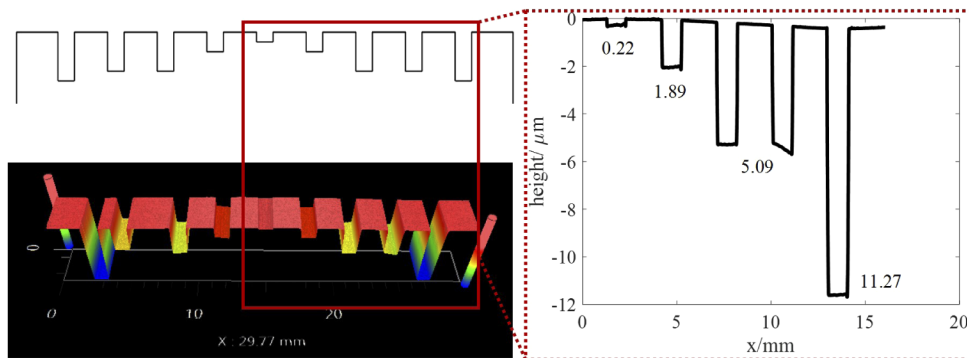


**Fig. 8.** Designed and manufactured four-step height artefact calibrated with Zygo.

enough information about the *z*-axis response curve, a step artefact with different heights can establish the relationship between the instrument response curve and the ideal one.

As shown in Fig. 8, a step surface with four different heights (0.2, 2, 5, 11) µm was designed and manufactured with an ultra-precision machining system from Moore Nanotech 350FG, USA. The manufactured step artefact was calibrated with a white light interferometer named Zygo Nexview, 5×.

The range of the *z*-axis of the displacement sensor is about 2 mm. The ISDP measurement results were compared to the calibrated multi-step artefacts. In order to ensure that all the measured positions were within the range of the instrument, the multi-step was measured in 50% of the instrument's working range. A total of five measurement tasks were performed to reduce the random measurement errors.

## 3. Experiments and discussion

### 3.1. Vibration evaluation of the in-situ measurement system

In order to check the influence of the vibrations caused by the dynamic behaviour in the measuring process, a series of tests was carried out with a calibrated flat surface along the raster axis (*x*-axis in this research). The laser probe can provide a scanning sampling frequency ranging from 1 kHz to 200 kHz. Considering the avoidance of any alias of the signals of interest and the measurement accuracy of the laser probe with different sampling frequencies, a relatively high frequency of 20 kHz was used to obtain the scanned workpiece and 1000 Hz was selected to analyze the signals.

Figure 9 shows the signal vibrations with different scanning speeds. $f = 0$ mm/min means that the signals were measured when the on-machine measurement system was in its static condition. As shown in Fig. 9, the vibration values for each scanning speed can be summarized as its standard deviation, which are listed in Table 1. The in-situ static vibration was less than 20 *nm*, but the values were significantly increased when the laser scanner was moved along the machine axis at a low speed which was up to almost 10 times the static value. On the contrary, it seems that the vibrations exhibited a sharp decrease down to 10 nm when the feed rate was increased to 2 mm/min. After that, the standard values ranged over a very small scale until the feed rate was increased to 8 mm/min. The vibration amplitude becomes large when the feed rate is increased to 8 mm/min, which may be caused by the integrated mechanical structure. The fixture which was used for holding the sensor was made of aluminium alloy, which is light in weight but has relatively lower stiffness compared with the material of the machine axes. It may cause vibration when the machine axes are moved at a high feed rate. According to the spectrum analysis of the vibration signal at different feed rates as shown in Fig. 10, the vibration amplitude was increased dramatically in the low frequency area (lower than 20 Hz) when the feed rate ranged from 0.5 to 8 mm/min. Furthermore, the spectrum analysis also indicated that the frequencies of the vibration signals were less than approximately 40 Hz. Hence, combining the consideration of values in the two figures (Fig. 9, Fig. 10) and the table (Table 1), the scanning speed would be better at about 6 mm/min, and the analyzed sampling frequency should be larger than 80 Hz on the condition that the requirement of surface feature frequency of the measured workpiece was met.

**Table 1. Standard deviation of the vibration signals with different moving speeds**

| Feed rate (mm/min) | 0 | 0.5 | 2 | 6 | 8 |
|---|---|---|---|---|---|
| Standard deviation (µm) | 0.02 | 0.17 | 0.09 | 0.08 | 0.11 |

### 3.2. Calibration of the z-axis scale errors

After obtaining the scanning speed of the on-machine system, a step surface with four steps was used to check the *z*-axis scale errors. The scanning speed was set as 6 *mm/min* along the *x*-axis
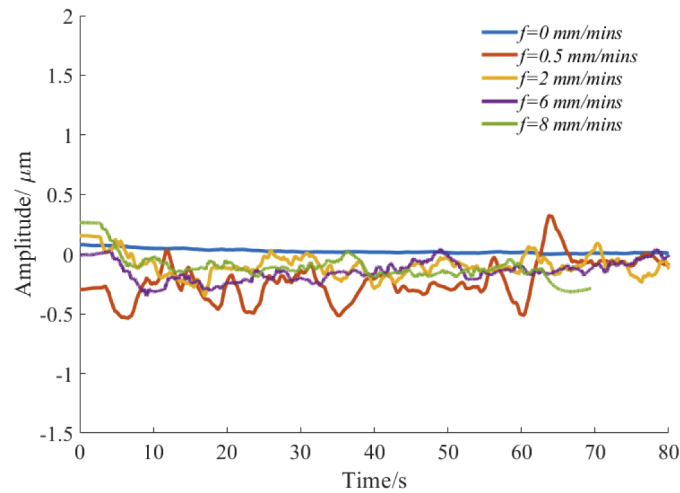
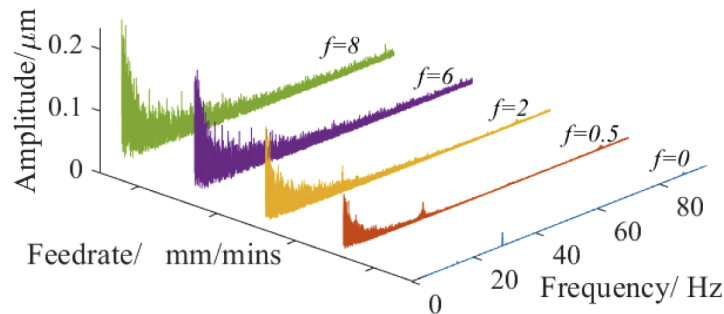**Fig. 9.** Dynamic vibrations of the measured signals with different scanning feed rates.



**Fig. 10.** Spectrum analysis of the vibration signal at different feed rates.

and three repeated measurements were carried out from $-16$ *mm* to $16$ *mm*. A fitted curve with different step heights is shown in Fig. 11, and the deviations between the measurement values obtained from the in-situ laser scanner and the off-machine Zygo Nexview are also listed in Table 2.

**Table 2. Measurement results of the step heights with both in-situ and off-machine methods**

| Zygo values (μm) | 0.22 | 1.89 | 5.09 | 11.27 |
|---|---|---|---|---|
| Laser scanner (μm) | 0.11 | 1.77 | 4.87 | 11.05 |
| Deviation (μm) | -0.11 | -0.12 | -0.22 | -0.22 |

By using the different step heights artefact and combining the measured results by the Zygo as a reference, the corrected amplification coefficient of the z-axis scale of the in-situ measurement system was about 0.9754, and the linearity deviation was less than 0.15 μm.

### 3.3. Volumetric error identification

Several experiments were conducted to check the developed mathematical model of volumetric positioning errors of the on-machine measurement system and the GP-based error prediction and compensation approach. The maximum measurement volume was approximately 200 mm × 40
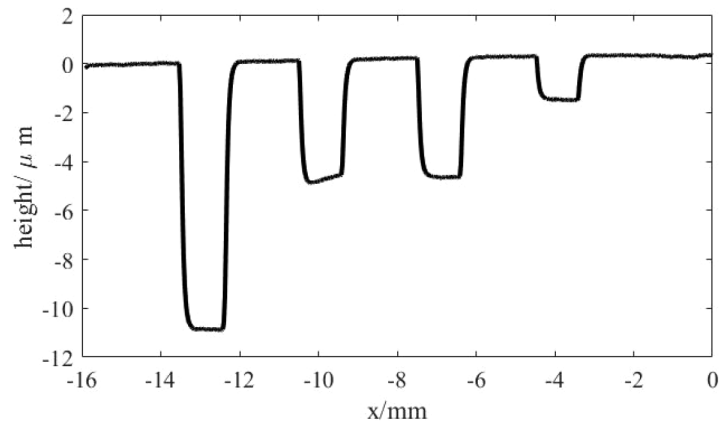
**Fig. 11.** Fitted curve of the step heights measured by the laser scanner.

mm × 50 mm. In order to ensure that the accuracy of the measurement was far less than the volumetric error, a total of 20 points were sampled uniformly in a 6 mm × 6 mm area and they were inspected three times.

As discussed before, 24 fiducials assembled on a fixture were randomly mounted in a 200 mm × 40 mm × 50 mm workspace. The fiducials were made of $Si_3N_4$ and acquired from the market. The positions of the fiducials were then calibrated in a multi-sensor Coordinate Measuring Machine named Werth Videocheck from Germany in a thermally controlled laboratory. The calibrated fiducial diameters were 9.997 ± 0.0002 mm, which indicated that the errors in the calibrated points were 0.2 μm. In the in-situ measurement system, the fixture with the calibrated fiducials was randomly mounted in the machine tool workspace. Hence, the positions of the fiducials were measured by the laser probe. After using the built chi-square volumetric error identification method, GP-based volumetric error prediction was used by setting the positions of the 24 fiducials and their volumetric position errors as the input. Figure 12 shows the measured positions of the fiducials and their volumetric errors. To improve the performance of the in-situ measurement system, the fixture with fiducials was controlled to move to 10 random positions in the machine tool.

Figure 13(a) shows the predicted 3D errors in the entire working space. Figures 13(b)–13(d) contain the other views of the volumetric errors. The mean value of the volumetric positioning
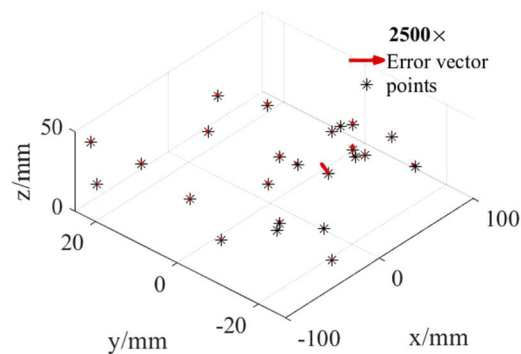


**Fig. 12.** (a) Positions of randomly selected 24 fiducials and their volumetric positioning errors (magnified 2,500 times).

errors is 1.2 μm and the prediction value is about 1.6 μm in the entire working space. These results indicate that the developed volumetric error prediction method can identify errors with high precision and error compensation followed by this method which can be easily carried out by modifying the tool path. It is worth noting that only a few measured points are needed but relatively high-accuracy results can be achieved.
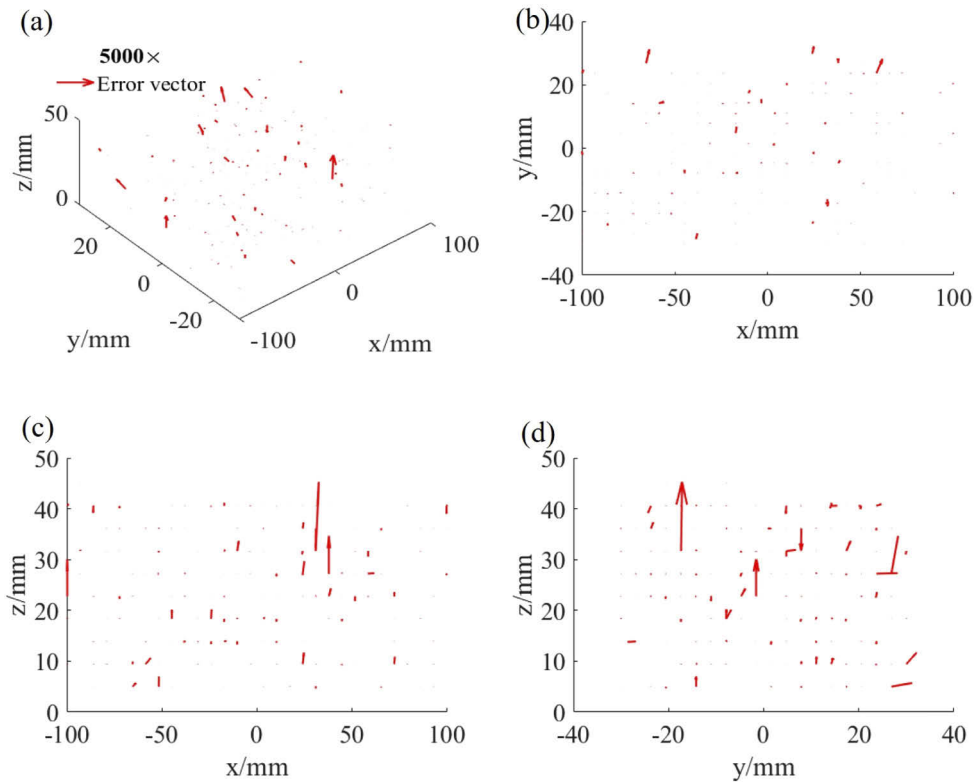


**Fig. 13.** (a) GP-based 3D volumetric error prediction in the working space (magnified 5,000 times) and (b) *xy* view (c) *xz* view (d) *yz* view.

## 3.4.  *Freeform surface in-situ measurement*

Two freeform surfaces were measured by the developed in-situ probing system. In order to check the accuracy of the probing system, a comparison with the measurement results obtained from the CMM (Werth Videocheck) was also carried out. The uncertainty of the CMM is $(0.25 + L/300)$ μm with a 0.2 mm fibre probe in a temperature range of $20 \pm 0.2°C$. In order to reduce the effect of temperature, the in-house temperature was also set at 20°C.

A relatively flat freeform F-theta surface and a sinusoidal surface with an amplitude of 0.5 mm as shown in Eq. (20) and Eq. (21) were employed to check the inspections. The two freeform surfaces were both machined by a fly-cutting machine tool as shown in Fig. 1.

$$z = \frac{-1}{250}x^2 + \frac{1}{92000}x^4 - \frac{1}{25}y^2, x \in [-15, 15], y \in [-5, 5] \tag{20}$$

$$z = 0.5(\sin(\pi/9x) + \cos(\pi/9y)), x \in [-8, 8], y \in [-8, 8] \tag{21}$$

Both surfaces were scanned at a 6 mm/min feed rate, and the raster was set as 0.5 mm. The measured data were obtained in a point cloud format with a down sampled 200 Hz sampling rate

from a 20 kHz sampling frequency of the laser scanner. The Iterative Closest Point (ICP) method [31] was used to carried out surface registration and the errors of the measured surface were characterized as the root-mean-square (RMS) and peak-to-valley (PV) values.

The characterized results of the two surfaces are illustrated in the 3D form error maps shown in Fig. 14. To present the whole measured surfaces, the 3D form error maps were reconstructed using the B-spline method. The compared results of the two surfaces are also summarized in Table 3.
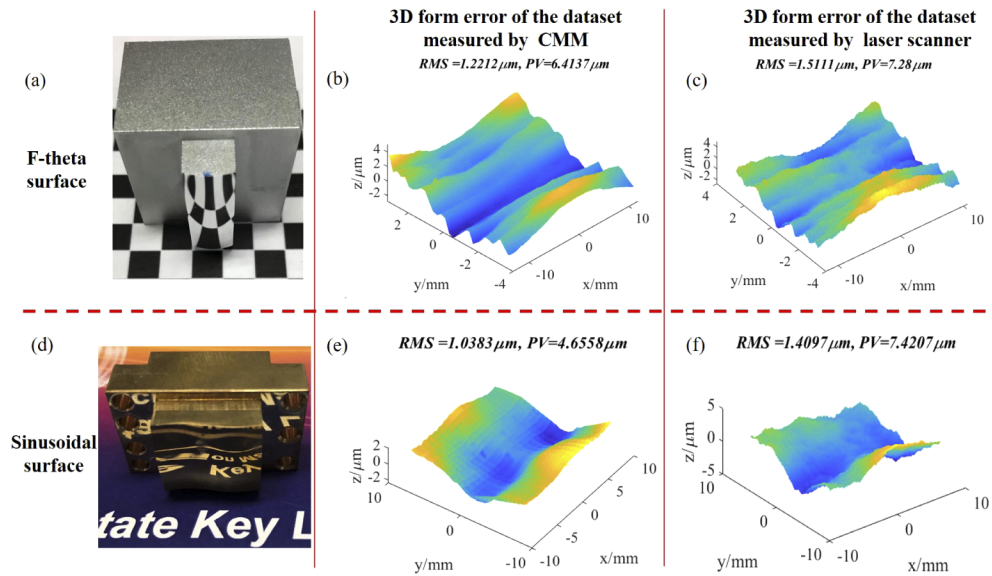


**Fig. 14.** (a) and (d) Workpiece of F-theta lens surface and sinusoidal surface, (b) and (e) 3D form error map of the dataset measured by CMM, (c) and (f) 3D form error map of the dataset measured by laser scanner, respectively.

**Table 3. Summary of the two measured surfaces**

| Surfaces | F-theta lens surface | | Sinusoidal surface | |
|---|---|---|---|---|
| Parameters | RMS | PV | RMS | PV |
| CMM values ($V_{cmm}$) (μm) | 1.22 | 6.41 | 1.04 | 4.66 |
| In-situ values ($V_{is}$) (μm) | 1.51 | 7.28 | 1.41 | 7.42 |
| ($V_{is}$-$V_{cmm}$)/$V_{cmm}$ | 0.248 | 0.136 | 0.356 | 0.592 |

As shown in Figs. 14(b), 14(c), 14(e) and 14(f), form errors of the in-situ measurement were almost consistent with that of the CMM inspections. However, according to Table 3, there was an increase of larger than 13.6% in RMS and PV values for both freeform surfaces. In addition, the measurement results at the relatively flat F-theta freeform surface had higher accuracy compared with those of the sinusoidal surface, and the increase of RMS of the former surface was up to 24.8% but the latter exhibited an almost 60% rise. The uncertainty of these measurement results may be caused by the reflection of the laser light at the steep slope of the surface, transformation errors between the machine tool coordinate frame and the in-situ measurement system as well as the imperfection of the laser scanner fixture and accuracy of the laser sensor. It is clear that higher measurement error occurs when a relatively complex surface is measured for the developed in-situ measurement although the volumetric error of the measurement system was compensated for. From these in-situ measurements, the calibrated in-situ coordinate measuring

system exhibited compatible performance in measuring freeform surface as compared with those of the high-accuracy CMM. These results may be enhanced by utilizing a more accurate laser sensor or better designed fixture.

## 4.  Conclusion

This paper presents a calibration strategy for an integrated in-situ displacement probing (ISDP) system on an ultra-precision fly-cutting machine tool. Three main error sources were analyzed and identified by both simulations and experiments. Two freeform surfaces were measured on the in-situ displacement probing system and the measured surface form errors demonstrate compatible performance of the developed ISDP system compared with traditional off-line measurement systems. The following observations can be drawn:

(i) Dynamic vibrations of the in-situ probing system are influenced by the scanning speed of the moving axes. Experimental studies show that most of the vibration frequencies were lower than 20 Hz when the feed rate ranged from 0 mm/min to 8 mm/min so that an optimized scanning speed and sampling frequency can be determined.

(ii) Volumetric positioning errors of the ultra-precision fly-cutting machine can be identified using a calibrated fiducial-aided artefact. Simulation showed that the optimized number of fiducials was 24.

(iii) Volumetric positioning error in the entire working space can be predicted by the proposed Gaussian process method. Simulations and experiments proved that the accuracy of the prediction model was lower than 0.0096 μm. The main error was about 1.6 μm in a 200 mm × 40 mm × 50 mm workspace.

(iv) Measurement of the multi-step heights was used to correct the z-axis scale errors; the corrected amplification coefficient was found to be about 0.9754 and the linearity error was less than 0.15 μm.

(v) Compared with the results measured on the high-precision multi-sensor CMM for the two freeform surfaces, the in-situ inspection exhibited greater measurement uncertainty. Moreover, the developed ISDP system appears to have better performance if the surface has relatively low geometric complexity.

There are some ways forward for further work. For example, the accuracy of the developed ISDP system is within micrometer range in terms of root-mean-square (RMS) and Peak-to-Valley (PV) values. Future research is suggested to be conducted to further enhance the robustness of the developed system by improving the stability of the integrated system, providing higher accuracy sensor and so on. Furthermore, although it is wise to use standard spheres as fiducials, other shapes of fiducials such as cones and cubes the features of which are worthy of further exploration regarding their possibility of enhancing the performance of the ISDP system.

## Disclosures

The authors declare no conflicts of interest.

## References

1. D. J. Whitehouse, "Comparison between stylus and optical methods for measuring surfaces," CIRP Ann. **37**(2), 649–653 (1988).
2. A. Ghiotti, A. Schöch, A. Salvadori, S. Carmignato, and E. Savio, "Enhancing the accuracy of high-speed laser triangulation measurement of freeform parts at elevated temperature," CIRP Ann. **64**(1), 499–502 (2015).
3. Z. Tong, W. Zhong, S. To, and W. Zeng, "Fast-tool-servo micro-grooving freeform surfaces with embedded metrology," CIRP Annals (2020).
4. D. Li, C. F. Cheung, M. Ren, D. Whitehouse, and X. Zhao, "Disparity pattern-based autostereoscopic 3D metrology system for in situ measurement of microstructured surfaces," Opt. Lett. **40**(22), 5271–5274 (2015).
5. X. Zhang, L. Jiang, and G. Zhang, "Novel method of positioning optical freeform surfaces based on fringe deflectometry," CIRP Ann. **66**(1), 507–510 (2017).
6. W. L. Zhu, S. Yang, B. F. Ju, J. Jiang, and A. Sun, "Scanning tunneling microscopy-based on-machine measurement for diamond fly cutting of micro-structured surfaces," Precis. Eng. **43**, 308–314 (2016).
7. D. Li, X. Q. Jiang, Z. Tong, and L. Blunt, "Development and application of interferometric on-machine surface measurement for ultraprecision turning process," J. Manuf. Sci. Eng. **141**(1), 014502 (2019).
8. D. Li, Z. Tong, X. Q. Jiang, L. Blunt, and F. Gao, "Calibration of an interferometric on-machine probing system on an ultra-precision turning machine," Measurement **118**, 96–104 (2018).
9. F. Chen, S. Yin, H. Huang, H. Ohmori, Y. Wang, Y. Fan, and Y. Zhu, "Profile error compensation in ultra-precision grinding of aspheric surfaces with on-machine measurement," Int. J. Mach. Tools Manuf. **50**(5), 480–486 (2010).
10. K. W. Lee, Y. J. Noh, W. Gao, Y. Arai, Y. Shimizu, K. Tanaka, M. Fukuta, and Y. Kai, "Experimental investigation of an air-bearing displacement sensor for on-machine surface form measurement of micro-structures," Int. J. Precis. Eng. Manuf. **12**(4), 671–678 (2011).
11. X. Zhang, Z. Zeng, X. Liu, and F. Fang, "Compensation strategy for machining optical freeform surfaces by the combined on-and off-machine measurement," Opt. Express **23**(19), 24800–24810 (2015).
12. B. Xu, Y. Shimizu, S. Ito, and W. Gao, "Surface profile measurement of internal micro-structures," Int. J. Precis. Eng. Manuf. **14**(9), 1535–1541 (2013).
13. S. Ito, D. Matsuura, T. Meguro, S. Goto, Y. Shimizu, W. Gao, S. Adachi, and K. Omiya, ""On-machine form measurement of high precision ceramics parts by using a laser displacement sensor," J. Adv. Mech. Design, Syst. Manuf. **8**(4), JAMDSM0048 (2014).
14. X. Chen, T. Nakamura, Y. Shimizu, C. Chen, Y.-L. Chen, H. Matsukuma, and W. Gao, "A chromatic confocal probe with a mode-locked femtosecond laser source," Opt. Laser Technol. **103**, 359–366 (2018).
15. J. Seewig, G. Beichert, R. Brodmann, H. Bodschwinna, and M. Wendel, *Extraction of shape and roughness using scattering light*, SPIE Europe Optical Metrology (SPIE, 2009), Vol. 7389.
16. S. Tereschenko and P. Lehmann, "Inline-fähige Weißlichtinterferometrie mit integrierter Schwingungskompensation/Inline scanning white-light interferomety with integrated vibration compensation," tm-Technisches Messen **85**(s1), s14–s20 (2018).
17. T. I. Murphy, "Line spacing in latex documents," retrieved 20,5, 2020, https://www.keyence.com/products/measure/laser.
18. S. X. Wang, C. F. Cheung, M. J. Ren, and M. Y. Liu, "Fiducial-aided on-machine positioning method for precision manufacturing of optical freeform surfaces," Opt. Express **26**(15), 18928–18943 (2018).
19. L.B. Kong, "Modeling of ultra-precision raster milling and characterization of optical freeform surfaces," The Hong Kong Polytechnic University, https://theses.lib.polyu.edu.hk/handle/200/5782 (2010).
20. S. X. Wang, B. Cheung, and M. J. Ren, "Uncertainty analysis of a fiducial-aided calibration and positioning system for precision manufacturing of optical freeform optics," Meas. Sci. Technol. **31**(6), 065012 (2020).
21. A. Wan, L. Song, J. Xu, S. Liu, and K. Chen, "Calibration and compensation of machine tool volumetric error using a laser tracker," Int. J. Mach. Tools Manuf. **124**, 126–133 (2018).
22. B. JCGM, "*101 2008 Evaluation of Measurement Data–Supplement 1 to the 'Guide to the Expression of Uncertainty in Measurement'—Propagation of distributions using a Monte Carlo method GUM*," (International Organisation for Standardisation, Geneva, 2008).
23. M. J. Ren, C. F. Cheung, and L. B. Kong, "A task specific uncertainty analysis method for least-squares-based form characterization of ultra-precision freeform surfaces," Meas. Sci. Technol. **23**(5), 054005 (2012).
24. A. G. Wilson, "*Covariance kernels for fast automatic pattern discovery and extrapolation with Gaussian processes*," (University of Cambridge, Cambridge, UK, 2014).

25. C. L. Giusca, R. K. Leach, and F. Helery, "Calibration of the scales of areal surface topography measuring instruments: part 2. Amplification, linearity and squareness," Meas. Sci. Technol. **23**(6), 065005 (2012).

26. R. K. Leach, C. Giusca, H. Haitjema, C. Evans, and X. Jiang, "Calibration and verification of areal surface texture measuring instruments," CIRP Ann. **64**(2), 797–813 (2015).

27. A. Kipnis, Y. C. Eldar, and A. J. Goldsmith, "Analog-to-digital compression: A new paradigm for converting signals to bits," IEEE Signal Process. Mag. **35**(3), 16–39 (2018).

28. M. Eifler, F. Schneider, J. Seewig, B. Kirsch, and J. C. Aurich, "Manufacturing of new roughness standards for the linearity of the vertical axis – Feasibility study and optimization," Eng. Sci. Technol., Intl. J. **19**(4), 1993–2001 (2016).

29. W. Bauer, D. Hüser, and D. Gerbert, "Simple method to determine linearity deviations of topography measuring instruments with a large range axial scanning system," Precis. Eng. **64**, 243–248 (2020).

30. ISO25178-601, "*Geometrical product specifications (gps)—surface texture: areal— part 601. Nominal characteristics of contact (stylus) instruments*," (Geneva:International Organization for Standardization, 2010).

31. M. Y. Liu, C. F. Cheung, C. H. Cheng, R. Su, and R. K. Leach, "A Gaussian process and image registration based stitching method for high dynamic range measurement of precision surfaces," Precis. Eng. **50**, 99–106 (2017).